International Journal of Nanomedicine

Dovepress

open access to scientific and medical research

Open Access Full Text Article

ORIGINAL RESEARCH

Layer-by-Layer Nanoparticles for Calcium Overload in situ Enhanced Reactive Oxygen Oncotherapy

Boye Zhang[1,2], Jianliang Man[3,4], Lingyun Guo[1], Xiaoxia Ru[1], Chengwu Zhang[1,2], Wen Liu[1,2,5], Lihong Li[1,2,5], Sufang Ma[1,2], Lixia Guo[2,4], Haojiang Wang[1,2], Bin Wang[1,2], Haipeng Diao[1,5], Renchao Che[6,7], Lili Yan[1,2,5]

[1]School of Basic Medical Sciences, Shanxi Medical University, Taiyuan, 030001, People's Republic of China; [2]Shanxi Province Brain Degenerative Diseases Precision Diagnosis and Treatment Engineering Research Center, Shanxi Medical University, Jinzhong, 030606, People's Republic of China; [3]Academy of Medical Sciences, Shanxi Medical University, Taiyuan, 030001, People's Republic of China; [4]College of Pharmacy, Shanxi Medical University, Taiyuan, 030001, People's Republic of China; [5]Key Laboratory of Cellular Physiology, Ministry of Education, Shanxi Medical University, Taiyuan, 030001, People's Republic of China; [6]Laboratory of Advanced Materials, Shanghai Key Laboratory of Molecular Catalysis and Innovative Materials, Academy for Engineering &Technology, Fudan University, Shanghai, 200438, People's Republic of China; [7]Zhejiang Laboratory, Hangzhou, 311100, People's Republic of China

Correspondence: Lili Yan; Renchao Che, Email yanlili@sxmu.edu.cn; rcche@fudan.edu.cn

Background: Challenges such as poor drug selectivity, non-target reactivity, and the development of drug resistance continue to pose significant obstacles in the clinical application of cancer therapeutic drugs. To overcome the limitations of drug resistance in chemotherapy, a viable treatment strategy involves designing multifunctional nano-platforms that exploit the unique physicochemical properties of tumor microenvironment (TME).

Methods: Herein, layer-by-layer nanoparticles with polyporous CuS as delivery vehicles, loaded with a sonosensitizer (tetra-(4-aminophenyl) porphyrin, TAPP) and sequentially functionalized with pH-responsive $CaCO_3$, targeting group hyaluronic acid (HA) were designed and synthesized for synergistic treatment involving chemodynamic therapy (CDT), sonodynamic therapy (SDT), photothermal therapy (PTT), and calcium overload. Upon cleavage in an acidic environment, $CaCO_3$ nanoparticles released TAPP and Ca^{2+}, with TAPP generating $^1O_2$ under ultrasound trigger. Exposed CuS produced highly cytotoxic ·OH in response to H_2O_2 and also exhibited a strong PTT effect.

Results: CuS@TAPP-$CaCO_3$/HA (CTCH) delivered an enhanced ability to release more Ca^{2+} under acidic conditions with a pH value of 6.5, which in situ causes damage to HeLa mitochondria. In vitro and in vivo experiments both demonstrated that mitochondrial dysfunction greatly amplified the damage caused by reactive oxygen species (ROS) to tumor, which strongly confirms the synergistic effect between calcium overload and reactive oxygen therapy.

Conclusion: Collectively, the development of CTCH presents a novel therapeutic strategy for tumor treatment by effectively responding to the acidic TME, thus holding significant clinical implications.

Keywords: mitochondria damage, calcium overload, reactive oxygen oncotherapy, pH-responsive, synergistic treatment

Introduction

Currently, cervical cancer is one of the most common gynecological malignant tumors, and the incidence of cervical cancer is gradually becoming younger.[1] Although chemotherapy for the treatment of cervical cancer has been the subject of intense research, cervical cancer remains a serious health problem for women worldwide.[2,3] Challenges arise due to insufficient drug selectivity, non-specific reactivity, and drug resistance leading to poor tumor treatment effect with therapeutic drugs.[4] Tumor microenvironment (TME) holds the key to tumor metastasis, angiogenesis and drug resistance.[5–7] Compared with normal physiological environment, tumor tissue has a more complex TME, which is characterized by hypoxia, acidic pH, excess of intrinsic H_2O_2, glutathione (GSH), and enzyme over expression.[8,9] The development of nanotechnology has led to the potential application prospects of integrating two or more therapeutic modalities into a single nanotherapeutic agent for synergistic treatment. These nanoplatforms utilize enhanced permeability and retention effects to improve therapeutic efficacy, reduce drug side effects, and achieve synergistic cancer therapy.[10,11] However, combination therapy often lacks specificity for

Received: 5 April 2024
Accepted: 8 July 2024
Published: 18 July 2024

the tumor site, leading to unnecessary damage to normal tissues. The design and development of TME-responsive smart nanoplatforms has garnered increasing attention in improving the efficacy of drug therapy, offering potential solutions to issues, such as poor treatment effect and serious side effects.[10,11] TME-activated nanocomplexes provide a precise targeted strategy for cancer therapy.

Mitochondria, which produce the majority of cellular energy in the form of adenosine triphosphate (ATP), have been involved in many other physiological processes, including controlling signal transmission, cell differentiation, and cell cycle. Therefore, a wide range of strategies have been developed to induce mitochondrial apoptosis in cancer cells.[12,13] Mitochondrial dysfunction can lead to cell death due to ATP deficiency, prompting the proposal of various strategies for stimulating mitochondrial apoptosis in cancer therapy. The antitumor effects of Ca^{2+} have led to increased attention on mitochondrial Ca^{2+} overload as a promising pathway for inducing mitochondrial dysfunction.[14,15] Therefore, mitochondrial Ca^{2+} overload presents a promising approach for targeting tumors.

Among various nanomaterials, $CaCO_3$ has become an attractive platform for constructing acid responses in tumors due to its excellent biocompatibility and inherent acid-induced decomposition.[16,17] Furthermore, under acidic conditions, the release of Ca^{2+} from $CaCO_3$ nanoparticles can elevate exogenous Ca^{2+} levels in cells, leading to severe mitochondrial dysfunction.[18] However, mitochondrial damage induced by a single exogenous Ca^{2+} overload is limited. Increased mitochondrial reactive oxygen species (ROS) generation is another major means for mitochondrial apoptosis. Therefore, exogenous ROS is critical to further destroy the calcium buffering capacity of mitochondria, resulting in mitochondrial dysfunction, blocking energy sources inside cancer cells, and thus inhibiting tumor growth.[19–21]

Chemodynamic therapy (CDT), which employs Fenton/Fenton-like catalysts to transform intracellular H_2O_2 into toxic OH for destroying cancer cells, has received considerable attention in tumor therapy.[22–24] However, inadequate H_2O_2 in tumor cells is detrimental to the effect of Fenton reaction, significantly weakening the production of ROS and consequently limiting the therapeutic effect of CDT. In addition, due to the active chemical nature of ROS, the short half-life, and it will be severely consumed before reaching the tumor site, resulting in poor anti-tumor effect and damage to normal tissues.[25,26] Therefore, ROS produced by a single CDT has a limited effect on killing cancer cells. Notably, Wibrianto et al synthesized a novel nano-catalyst (CuCGC) capable of generating a substantial quantity of ROS when exposed to H_2O_2 and glucose, thereby significantly augmenting the efficacy of cancer treatment through combined CDT and starvation therapy (ST).[27]

Sonodynamic therapy (SDT), as a promising non-invasive tumor clearance strategy, uses US-triggered sensitizers to produce highly cytotoxic ROS that kill tumor cells. SDT can cooperate with CDT to generate more ROS and play an anti-tumor role.[28,29] However, most reported SDT materials are small molecular organic materials, which show strong cytotoxicity.[30–32] Photothermal therapy (PTT) is a minimally invasive treatment strategy that converts light energy into heat energy, induces apoptosis of cancer cells, and enhances tumor cell metabolism and membrane permeability.[33–35] Although some nanomaterials show great potential in PTT-based synergistic therapeutics, however, the therapeutic effects of PTT in tumor therapy are still limited, including poor photothermal conversion efficiency, material instability, and poor cell uptake.[36–39] The construction of TME-responsive nanodelivery platform can greatly reduce drug toxicity. For example, Korupalli et al developed a multifunctional nanocomposite material (MBIG NCs) that achieves enhanced therapeutic effectiveness by leveraging the synergistic interplay among starvation therapy, chemodynamic therapy, and phototherapy.[40] Therefore, it is of great significance to construct a response to TME the release of exogenous Ca^{2+} and the production of excess ROS synergistic nanomedicine, resulting in mitochondrial apoptosis to achieve tumor therapy.

In this work, a multifunctional nanomedicine (CuS@TAPP-$CaCO_3$/HA, CTCH) was designed and developed based on the acidic TME. To improve the water solubility of the materials, hyaluronic acid (HA) was loaded by electrostatic adsorption. Additionally, tetra-(4-aminophenyl) porphyrin (TAPP) and Ca^{2+} are released from $CaCO_3$ under an acidic environment. The released TAPP can produce $^1O_2$ when triggered by ultrasound. CuS, as Fenton-like nanomaterials, can produce highly cytotoxic OH in the presence of H_2O_2, enhancing effective PTT effects. Results indicated that the designed CTCH could realize the synergistic treatment of mitochondrial damage caused by CDT, SDT, PTT and calcium overload Scheme 1.

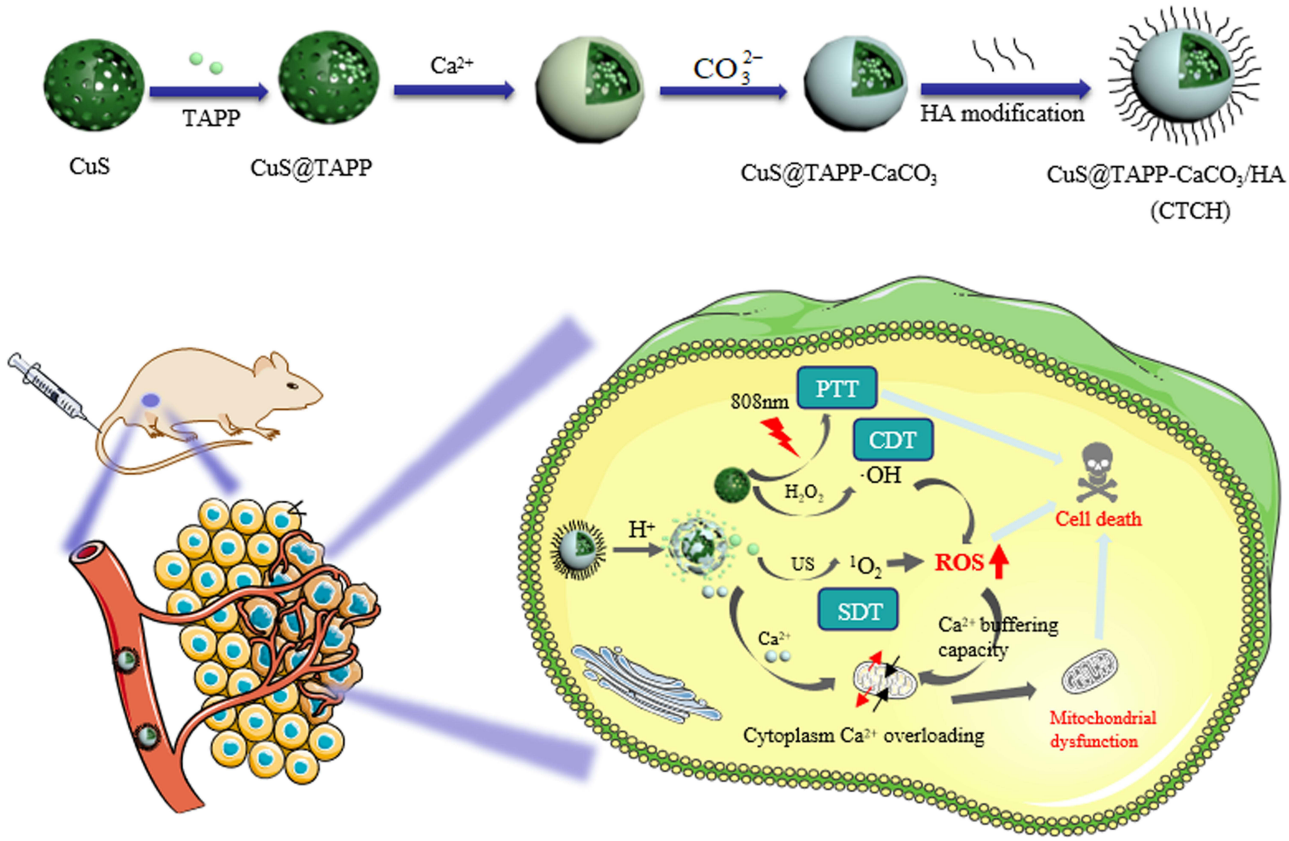

Scheme 1 Schematic diagram of the preparation process of CTCH and the combination of PTT, CDT and SDT for synergistic antitumor therapy.

Experimental Section

Materials and Apparatus

Copper chloride, dihydrate, hydrazine hydrate (80%), sodium hydroxide, calcium chloride, anhydrous sodium carbonate, HA, Rhodamine B (RhB), methylene blue (MB), and 3.3 ‘,5,5 ‘-tetramethylbenzidine (TMB) were obtained from Shanghai Maclin Biochemical Co., Ltd (Shanghai, China). Calcium ion detection kit was purchased from Shanghai Biyuntian Biotechnology Co., Ltd (Shanghai, China). Dulbecco’s Modification of Eagle’s Medium (DMEM), the methyl thiazole tetrazolium (MTT), calcein-AM, 2, 7-dichlorohydrofluorescein diacetate (DCFH-DA), and propyl iodide (PI) were provided by Beijing Solarbio Science & Technology Co., Ltd (Beijing, China). All of the cell lines used in our study were provided by the Cell Bank of the Chinese Academy of Sciences (Shanghai, China).

The absorption spectrum was acquired by a UV-vis spectrophotometer (UH-5300, Hitachi, Japan). The OD values of cytotoxicity were determined by a microplate reader (ELx808, BioTek, USA). Cell images were obtained under confocal laser scanning microscopy (FV3000, Olympus, Japan). The zeta potential and particle size of the nanomedicine were measured by the Nano particle size and zeta potential analyzer (Malvern ZEN3700, Britain). The morphological characteristics of CDs were measured by high-resolution transmission electron microscopy (TEM, Tecnai G2 F20 S-Twin, FEI, USA). Infrared imaging was measured with the thermal infrared instrument (PS 400, Guide sensmart, China). Fourier transform infrared spectroscopy (FTIR, Bruker OPTIK GmbH Tensor 27, Germany) and X-ray photoelectron spectroscopy (XPS, Thermo Scientific ESCALAB 250Xi, America) were used to detect the surface functional groups of the samples.

Preparation of CuS

About 300 μL $CuCl_2 \cdot 2H_2O$ solution (0.5 M) was added to 75 mL deionized water containing 0.72 g polyvinylpyrrolidone. Then, 75 mL of sodium hydroxide (pH 9.0) was added, followed by adding 19.2 μL hydrazine monohydrate ($N_2H_4 \cdot H_2O$) to

form a bright yellow solution. After the reaction for 5 min, 600 μL sodium sulfide aqueous solution (320 mg/mL) was added, and the solution was heated in an oil bath at 60°C for 2 h. Finally, the product was centrifuged at 12000 rpm for 8 min, washed with deionized water and alcohol, and dried to obtain the final nanomaterial.

Preparation of CuS@TAPP

9.5 mg CuS dissolved in 4.5 mL deionized water and 2.3 mg TAPP dissolved with 0.5 mL DMSO were transferred to a 25 mL round-bottomed flask and reacted at 40°C and kept away from the light for 48 h. After centrifugation at 10000 rpm for 10 min, wash with deionized water several times until the supernatant was colorless.

Preparation of CuS@TAPP/$CaCO_3$-HA

The mixture solution of CuS@TAPP (600 μL, 5 mg/mL), $CaCl_2$ (320 μL, 5 mg/mL), and water (8 mL) continued stirring for 10 min. Na_2CO_3 (0.768 mL, 2 mg/mL) solution was added drop by drop to the mixture solution under continuous stirring for 10 min. Finally, HA solution (2 mL, 5 mg/mL) was added to the mixture solution above and stirred for 24 h. After this, centrifuge and collect the precipitate, wash, and dry.

OH Detection by TMB

Experiment 1: Three groups of acetate buffer reaction system with a total volume of 2 mL were set up as follows: 10 μL TMB (0.8 M), 10 μL TMB (0.8 M) + H_2O_2 (2.5 mM), 10 μL TMB (0.8 M) + H_2O_2 (2.5 mM)+20 μL CTCH (5 mg/mL). According to with or without CTCH, they were divided into the experimental group and the control group.

Experiment 2: The concentrations of TMB and H_2O_2 were kept constant (0.8 M and 2.5 mM, respectively) in an acetate buffer reaction system with a total volume of 2 mL, while the concentrations of CTCH were 25 μg/mL, 50 μg/mL, and 100 μg/mL, respectively.

Experiment 3: The effects of H_2O_2 concentrations on ROS generation were tested by TMB. The concentrations of TMB and CTCH were kept constant (0.8 M and 50 μg/mL, respectively) in an acetate buffer reaction system with a total volume of 2 mL, while the H_2O_2 concentration was changed to 1 mM, 2.5 mM and 5 mM respectively.

Finally, the above-mentioned systems were incubated in a shaker at 37°C for 10 min. Following centrifugation, the supernatant was collected to observe the color. The absorbance at 652 nm was detected by a UV-vis spectrophotometer.

MB Detection OH

Experiment 1: Three phosphate-buffered saline (PBS) reaction systems (pH = 6.5) with a total volume of 2 mL were set up as follows: MB (10 μg/mL), MB (10 μg/mL) + H_2O_2 (10 mM), MB (10 μg/mL) +H_2O_2 (10 mM)+ CTCH (50 μg/mL). According to with or without CTCH, they were divided into the experimental group and the control group. Additionally, in the experimental group, the effects of pH (pH = 5.0, pH = 6.5, and pH = 7.4) on MB degradation were studied.

Experiment 2: The concentrations of MB and H_2O_2 were kept constant (10 μg/mL and 10 mM, respectively) in PBS reaction systems with a total volume of 2 mL, while the concentrations of CTCH were 0 μg/mL, 50 μg/mL, 100 μg/mL, 150 μg/mL, and 200 μg/mL, respectively.

Experiment 3: The effects of H_2O_2 concentrations on MB degradation were further studied. The concentrations of MB and CTCH were kept constant (10 μg/mL and 50 μg/mL, respectively) in PBS reaction systems with a total volume of 2 mL, while the H_2O_2 concentration was changed to 0 mM, 5 mM and 10 mM, respectively.

Experiment 4: The effects of temperature on MB degradation were explored. Four PBS reaction systems (pH = 6.5) with a total volume of 2 mL were set up as follows: MB (10 μg/mL), MB (10 μg/mL) + H_2O_2, and CTCH under different temperature (25°C, 37°C or 50°C).

Finally, the above-mentioned systems were incubated in a shaker for about 1 h. Following centrifugation, the supernatant was collected to observe the color. The absorbance at 665 nm was detected by a UV-vis spectrophotometer.

Detection of Release Ca^{2+}

67 μL CTCH (3 mg/mL) was placed in a 1.5 mL centrifuge tube, and PBS with different pH (pH = 7.4, pH = 6.5, or pH = 5.0) was prepared into a 2 mL solution. The solution was divided into three portions and then the solution was placed in a shaker at

140 rpm and 37°C for different reaction times (0 h, 0.5 h, 1 h, 5 h, 8 h, or 24 h). After centrifugation, 67 μL of supernatant was transferred to a centrifuge tube, and 67 μL of PBS was added into the solution system. Finally, 10 μL of the collected supernatant was added to the 96-well plate, followed by adding 250 μL of the configured Ca^{2+} test solution. Five minutes later, OD value was measured at 610 nm with an enzyme marker. To detect Ca^{2+} in solution, the standard Ca^{2+} concentration in the Ca^{2+} detection kit was tested for a standard graph.

Cell Uptake Assay

RhB was reacted with CTCH for 24 h by electrostatic adsorption, and the precipitation was treated by centrifugal washing to obtain fluorescently labeled CTCH. HeLa cells and human cervical epithelial cells (HcerEpic cells) were cultured in confocal dishes (1×10^5 cells/dish) and cultured for 24 h. The medium was discarded and cells were washed twice with PBS. CTCH (50 μg/mL) prepared with DMEM was added to each confocal dish and incubated for 0 h, 1 h, 2 h, 4 h, and 6 h, respectively. Finally, the cells were fixed with paraformaldehyde, stained with DAPI, and photographed with a laser confocal microscope.

MTT Assay

HcerEpic cells and HeLa cells were seeded in 96-well plates (8000 cells/well) and cultured in cell incubators. After 24 h of culture, the medium was discarded and CTCH (0 μg/mL, 10 μg/mL, 20 μg/mL, 30 μg/mL, 40 μg/mL, or 50 μg/mL) and TAPP (0 μg/mL, 1 μg/mL, 2 μg/mL, 3 μg/mL, 4 μg/mL, or 5 μg/mL) were added to each well. Then, the medium was discarded after 12 h culture and cells were washed twice with PBS. Add MTT 20 μL (0.5 mg/mL) to per well. After incubation for 4 h, MTT medium was removed. Then add 150μL DMSO. Finally, the OD value was detected at 490 nm using a microplate reader, and the cell survival rate was calculated.

Detection of Intracellular ROS and Mitochondrial Membrane Potential

Seven groups were set up as follows: Control, CTCH, CTCH + Vc, CTCH + L, CTCH + US, CTCH + L + US and CTCH + L + US (pH = 6.5). HeLa cells were seeded into 6-well plates (1×10^5 cells/well) for 24 h. Subsequently, the control group was added with 1 mL DMEM culture medium, and the other 6 groups were added with 1 mL of CTCH (50 μg/mL). After incubation for 6h, the corresponding groups were irradiated with an 808 nm laser for 10 min, treated with ultrasound for 5 min, or treated with synergistic therapy, respectively.

ROS detection: the above-mentioned media were removed and replaced with 1 mL PBS solution containing 10 mM DCFH-DA for intracellular ROS Detection. After incubation for 30 min, the fluorescence intensity of DCF was used to evaluate the ROS production performance.

Mitochondrial membrane potential detection: the above-mentioned media were removed and replaced with 1 mL of PBS solution containing JC-10 for detection of mitochondrial membrane potential (MMP). After incubation for 30 min, the influence of material on the MMP was evaluated.

In vivo Photothermal Effect

HeLa cells were subcutaneously injected into the right armpit of the Balb/c nude mice. When the tumors grew up to about 100 mm^3, the CTCH (20 mg/kg) was i.v. injected into the mice through the tail vein. After 8 h of treatment, the mice were anesthetized and irradiated with an 808 nm laser with 1.5 W/cm^2 for 10 min. The temperature changes were recorded by a thermal imager for every 2 min.

In vivo Evaluation of Therapeutic Effects

When the tumors grew up to about 100 mm^3, the mice were randomly assigned to the six groups: PBS, PBS + L + US, CTCH, CTCH + L, CTCH + US, and CTCH + L + US. The laser and the ultrasound group were irradiated with an 808 nm laser with 1.5 W/cm^2 for 10 min and treated with ultrasound at a power of 0.8 W/cm^2 for 5 min twice within 14 days, respectively. The health condition of nude mice in all groups was observed once every 2 days, and photographs were taken once every 7 days during the 14-day treatment period, respectively. During this period, tumor volumes and body weights of nude mice were monitored and recorded.

Biochemical Index Detection

After treatment, the orbital blood was collected from anesthetized mice. Subsequently, after centrifugation for 10 min at 3000 rpm, the upper serum was collected. The levels of aspartate aminotransferase (AST), alanine aminotransferase (ALT), urea nitrogen (BUN), and creatinine (Cr) were detected by biochemical assay kits, respectively.

Hemolysis Assay

Orbital blood was centrifuged and blood cells were isolated. The concentration of red blood cells in each group was the same. The positive control group was added with deionized water, and the other groups were treated with different concentrations of CTCH. The absorbance at 570 nm was measured using a microplate reader and the hemolysis rate was calculated.

H&E Staining of Organ Tissues

After euthanizing the mice, the major organs and tumor tissues were collected, photographed, weighed, and fixed with 4% paraformaldehyde for 24 h. After dehydration, embedding, ultrathin section, and H&E staining, the stained sections were observed and photographed under a laser confocal microscope.

Statistical Analysis

The values were expressed as the mean ± standard deviation. Statistical significance was determined using t-tests for two-group analysis, while one-way ANOVA for multiple group comparisons.

Results and Discussion

Characterization of CTCH

As can be seen from the TEM images (Figures 1A and S1A), the resultant CuS showed a high degree of homogeneity, a near-spherical shape with hollow mesopores and a physical particle size of approximately 128 nm. After coating with $CaCO_3$, there were obvious tiny nanosheets around CuS (Figure 1B). The final CTCH nanometer complex physical size was about 178 nm. The hydrodynamic dimensions of CuS and CTCH were approximately 146.5 nm (Figure S1B) and 215.4 nm (Figure S1C), respectively. The elemental mapping images of CTCH under TEM demonstrated the homogeneous distribution of Cu, S, Ca, C, and O (Figure 1C) inside CTCH, with well-overlapping merged images of Cu and Ca elements, further confirming high homogeneity. These results indicate that the prepared CTCH exhibits uniform spherical morphology and high purity.

From FTIR (Figure 1D), it was evident that the characteristic peak associated with the saccharide group appeared at 1038 cm^{-1}, confirming the successful coating of HA. XPS results (Figures 1E and S3) revealed that CTCH contained six elements (Cu, S, Ca, C, N, and O). The peaks of Ca 2p at binding energies, 351 and 347 eV corresponded to Ca 2p1/2 and Ca 2p3/2, indicating the presence of $CaCO_3$. The Cu 2p and S-Cu of Cu and S elements were observed at binding energies of 951 and 161 eV, respectively, suggesting the presence of CuS.

As depicted in Figure S1D, CuS exhibited a broad peak in the near-infrared region (NIR), indicating successful synthesis of CuS.[41,42] The characteristic absorption peak of CTCH at 420 nm, which similar with TAPP suggests the successful synthesis of CTCH. This finding further indicates the extensive absorption properties of CTCH as a photothermal material.

Furthermore, the zeta potentials of CuS, CuS@TAPP and CTCH were detected (Figure 1F). The surface potential of CuS was determined to be −16.26 mV. When TAPP was loaded into the pores of CuS, the potential changed to −12 mV. $CaCO_3$ was coated on CuS@TAPP surface and HA was then modified on the surface by electrostatic action to improve the biocompatibility of CTCH, the potential changed to −19.1 mV. The changes in Zeta potential further verify the successful preparation of CTCH. According to the characteristic absorbance of TAPP (Figure S2A and B), the drug loading of TAPP is 10.4 wt%. The high loading of TAPP may be due to the negative surface potential of CuS particles.

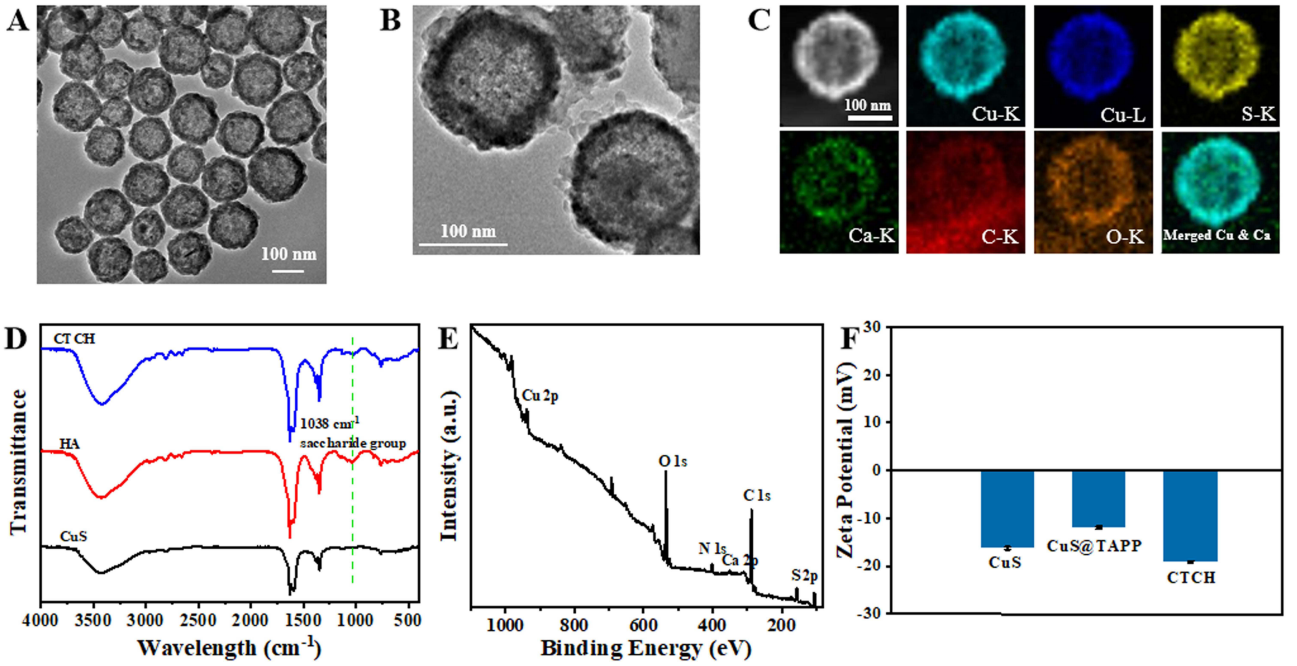

Figure 1 Characterizations of CTCH. (**A**) Low-magnification TEM image of CuS (scale bar: 100 nm); (**B**) TEM image of CTCH (scale bar: 100 nm); (**C**) Element mapping of CTCH (scale bar: 100 nm); (**D**) FTIR spectra of HA, CuS, and CTCH; (**E**) XPS spectra of CTCH; (**F**) Zeta potentiogram of CuS, CuS@TAPP and CTCH.

Photothermal Property

To intuitively understand the photothermal properties of CTCH, an infrared thermal imager was used to obtain thermal pictures and record the temperature changes under different concentrations and laser power.

Under laser irradiation, the temperature gradually increased as the concentration of CTCH increases (Figure 2A). When the concentration of CTCH was 200 μg/mL, the temperature of the CTCH increased from 26°C to 59.6°C after 5 min irradiation with 808 nm laser (Figure 2B). The infrared thermal imager captured temperature changes under 808 nm laser irradiation at 0.5 W/cm^2, 1.0 W/cm^2, and 1.5 W/cm^2 power densities (Figure 2C). Figure 2D indicates a positive correlation between the temperature variation of CTCH and the laser power. After 808 nm laser irradiation (1.5 W/cm^2), the temperature of the CTCH increased from 26°C to 72°C, indicating a good photothermal effect of the CTCH. The laser power density used in the subsequent cell and in vivo experiments was 1.5 W/cm^2. As a photothermal agent, the photothermal stability of CTCH was also crucial for tumor treatment. As shown in Figure 2E, the temperature curve of CTCH during four cycles laser irradiation was essentially unchanged, which reveals the good photothermal stability of prepared CTCH.

The Ca^{2+} Release and ROS Production in CTCH

Since ·OH can effectively degrade organic dyestuffs, we used TMB and MB to investigate the generation of ·OH from Fenton reaction system. Compared to the TMB and TMB + H_2O_2 groups, there was an obvious absorption peak at 652 nm after adding CTCH, indicating that CTCH could produce ·OH for tumor therapy (Figure 3A). Subsequently, different concentrations of CTCH were studied (Figure 3B) and the absorbance at 652 nm became stronger with the increasing concentration of CTCH. This finding indicates that the production of ·OH was related to the concentration of CTCH. Finally, the effects of H_2O_2 content on ·OH production were investigated and the results are shown in Figure 3C, demonstrating the positive correlation between the content of H_2O_2 and the production of ·OH.

MB was also used as an indicator for detecting ·OH. Compared to the MB and MB + H_2O_2 groups, the absorbance of MB significantly decreased after adding CTCH. Moreover, in acidic conditions (pH = 6.5) (Figure S4A), the degradation rate of MB was also increased. At the same time, MB was also used to detect the influence of the CTCH concentration on ·OH (Figure S4B). The higher the concentration of CTCH with the higher the absorbance at 665 nm indicates that the

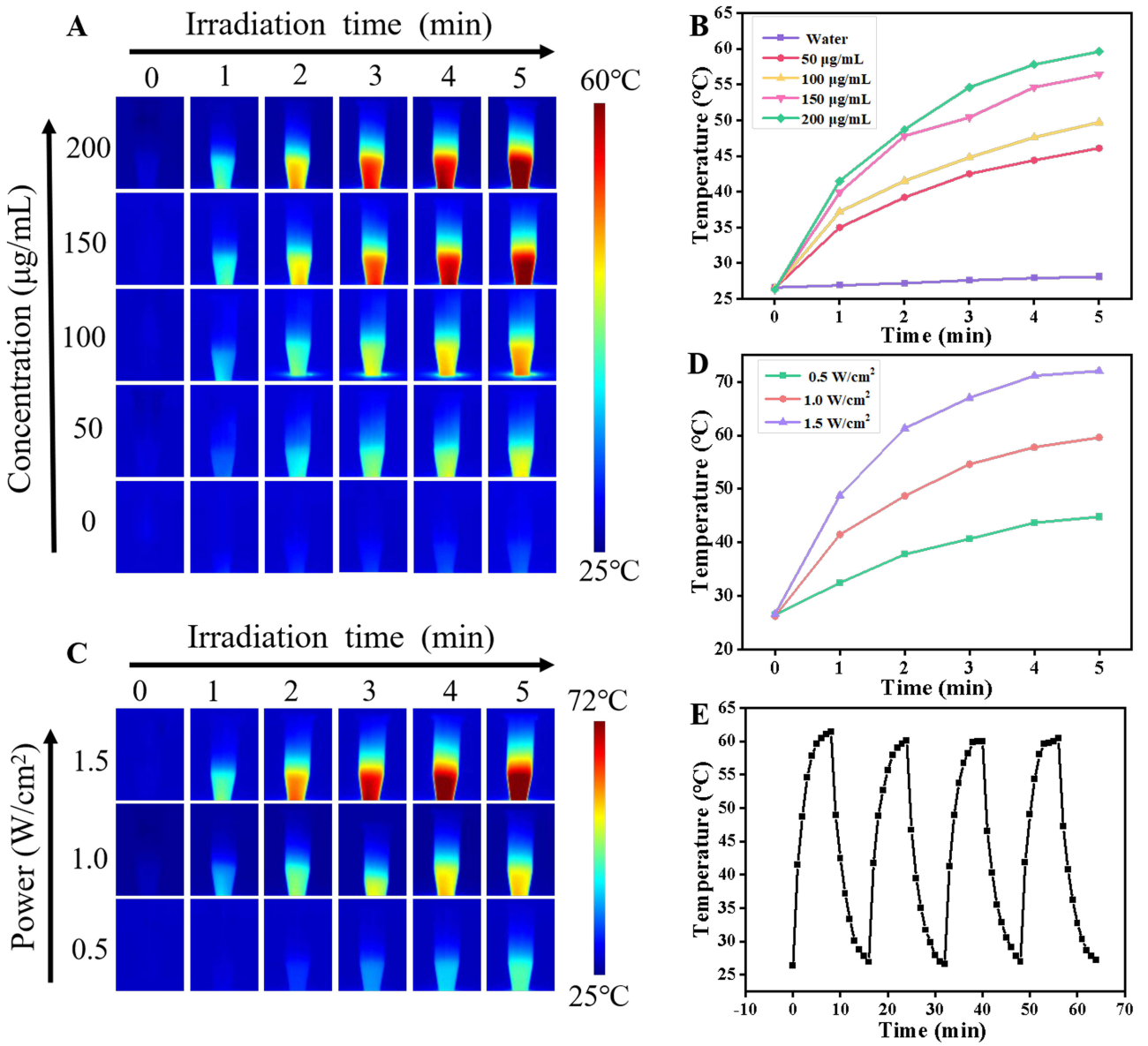

Figure 2 Evaluation of photothermal properties of CTCH. (**A**) Infrared imaging and (**B**) temperature-time plot of CTCH at different concentrations irradiated by 808 nm (1.0 W/cm^2) laser for 5 min; (**C**) Infrared imaging and (**D**) temperature-time plot of CTCH (200 μg/mL) irradiated by 808 nm laser at different laser powers for 5 min; (**E**) Photothermal heating curves of CTCH solution (200 μg/mL) upon exposure to 808 nm laser irradiation (1.0 W/cm^2).

generation of OH was related to the material concentration. Finally, the influences of temperatures and H_2O_2 content on ·OH were investigated (Figure S4C and D). The results indicate that the temperature could accelerate the catalytic reaction rate, and the H_2O_2 content was correlated positively with the production of ·OH.

Notably, compared to normal tissue, the H_2O_2 level in the tumor microenvironment is elevated at approximately 0.1–1mM.[43] MB was employed as a •OH trapping probe to further assess the catalytic activity of CTCH in the presence of low concentrations of H_2O_2. As H_2O_2 concentration increased, MB absorption gradually decreased, indicating that the formation of •OH was H_2O_2 concentration-dependent. Remarkably, after irradiation with an 808 nm laser (Figure S5), MB degradation was significantly enhanced, suggesting that heat generated by this laser may accelerate ROS production-thereby synergistically promoting the CDT process through the photothermal properties exhibited by CTCH.

Under acidic conditions, $CaCO_3$ in CTCH can release Ca^{2+}. Therefore, Ca^{2+} assay kits were used to detect the release of Ca^{2+} at different pH values. Figure S6 showed the Ca^{2+} standard curve of the kit. As the acidity of the solution increased, more Ca^{2+} was released (Figure 3D). Along with the extension of time, the Ca^{2+} release entered the plateau

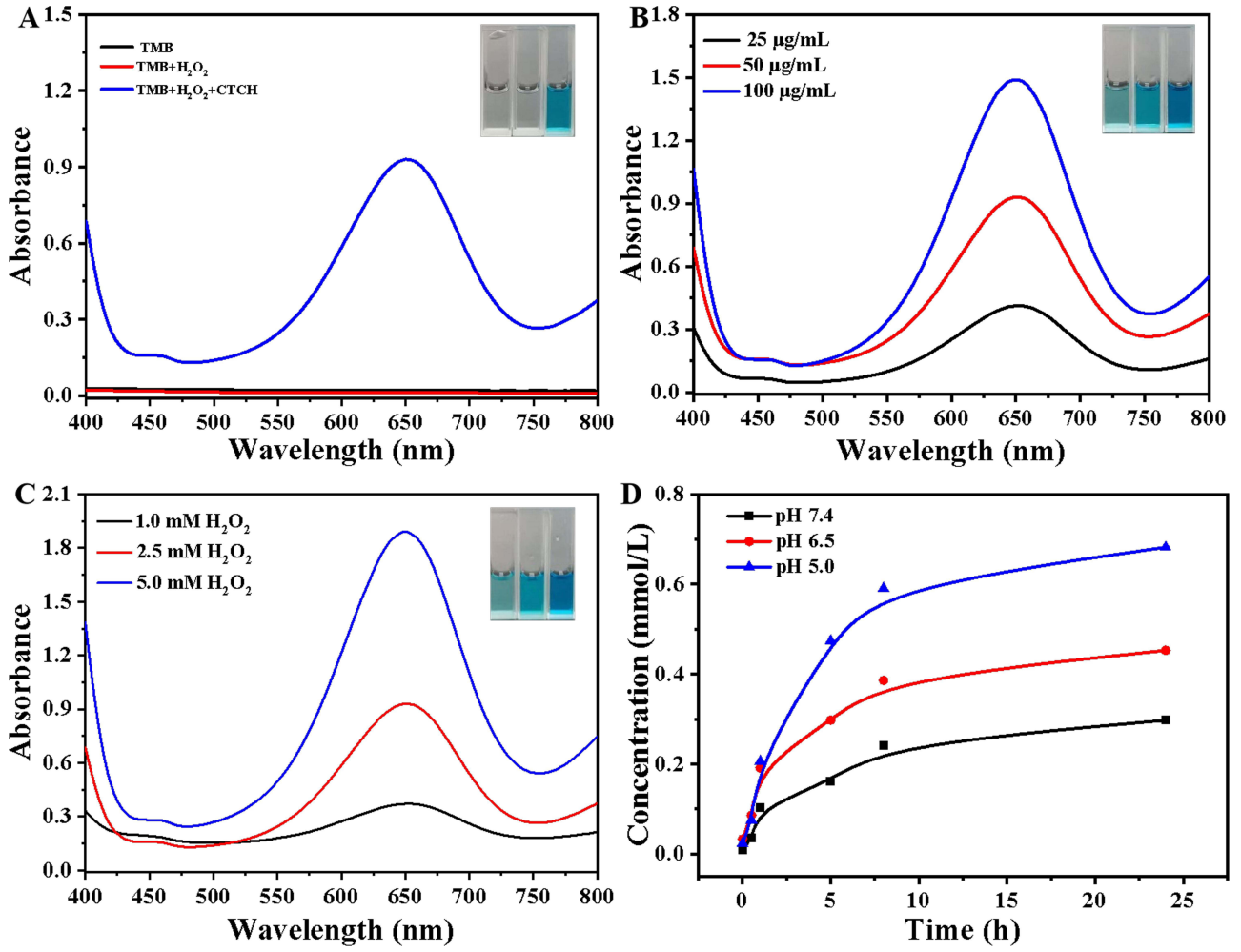

Figure 3 The performance of CTCH. UV-visible absorption spectra of TMB after co-incubation of (**A**) CTCH, (**B**) different concentrations CTCH and (**C**) CTCH with H_2O_2; (**D**) Ca^{2+} release curve under different pH conditions.

period. This indicates CTCH will produce a large amount of exogenous Ca^{2+} when entering cells under an acidic environment in TME, leading to intracellular calcium overload and assisting cancer therapy.

Detection of Intracellular ROS

The CTCH was labeled with RhB for CTCH uptake detection by HeLa cells. As shown in Figure S7, fluorescence imaging was obtained by an immunofluorescence microscope. With the increase of the incubation time, the fluorescence intensity gradually increased and reached its peak 4 h after cell uptake of CTCH. Additionally, how CTCH was taken up by cells through receptor-mediated endocytosis was further studied. Excess free HA was used to treat HeLa cells in culture for blocking the CD44-mediated pathway. After 4 h culture with Rhodamine B (RhB)-labeled CTCH, fluorescence images were obtained with fluorescence microscope. As shown in Figure S8, the red fluorescence intensity was significantly stronger in the RhB-labeled CTCH without free HA group than in the RhB-labeled CTCH with free HA group, indicating that CTCH interacts specifically with the overexpressed CD44 receptor on HeLa cells.

A commercial fluorescent probe DCFH-DA was used to examine the intracellular ROS production of CTCH. Compared with the control group (Figure 4A), fluorescence can be detected in the cells of the CTCH + Vc group, indicating that Ca^{2+} could inhibit mitochondrial activity, and thus produce small amounts of ROS. Compared with the CTCH + Vc group, the fluorescence intensity of the CTCH group has been enhanced remarkably, thereby indicating the effect of CTCH on CDT. In contrast, the green fluorescence of the CTCH + L group was enhanced, indicating that the photothermal treatment of CTCH could effectively

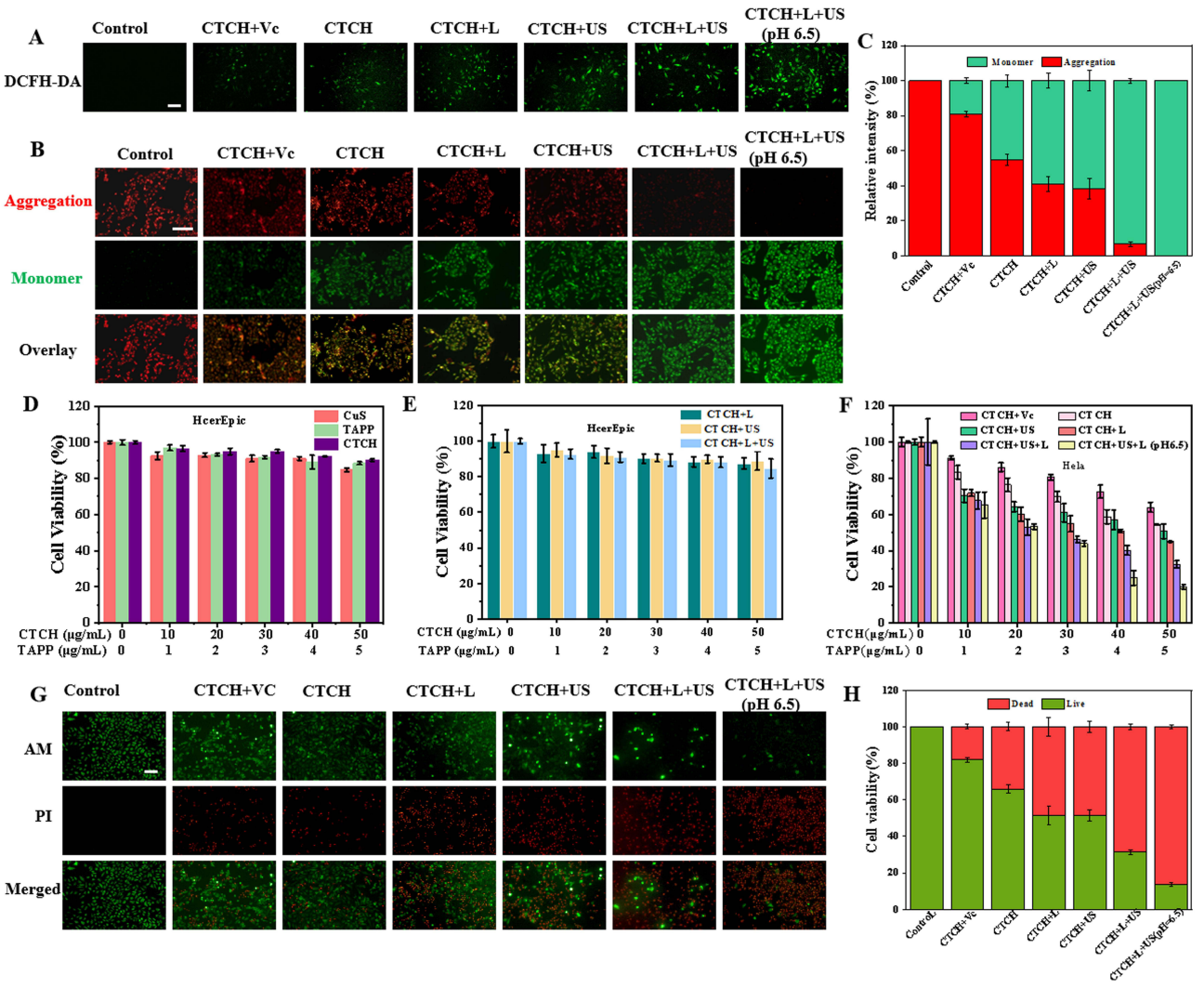

Figure 4 In vitro therapy evaluation. (**A**) The fluorescence images of HeLa cells stained with DCFH-DA (scale bar: 100 μm); (**B**) The fluorescence images of HeLa cells stained with JC-10 (scale bar: 50 μm); (**C**) Fluorescence intensity statistics corresponding to (**B**); (**D**) Effects of different concentrations of CuS, TAPP and CTCH on HcerEpic cell survival rate; (**E**) The effects of different concentrations of CTCH on the survival rate of HcerEpic cells after ultrasonic or laser treatment; (**F**) The effects of different concentrations of CTCH on the survival rate of HeLa cells under different conditions; (**G**) The fluorescence images of HeLa cells stained by calcein AM (green) and PI (red) after different treatments (scale bar: 100 μm); (**H**) Fluorescence intensity statistics corresponding to (**G**).

promote the production of ROS. The green fluorescence of the CTCH + US group was also enhanced compared with that of the CTCH group, indicating that CTCH had SDT property and ROS generation ability. The CTCH + L + US group showed strong green fluorescence, indicating that the calcium overload and the synergistic effect of CDT/PTT/SDT could produce a large number of ROS. Compared with the CTCH + L + US group, the red fluorescence of the CTCH + L + US group (pH = 6.5) was further enhanced. These results indicate that more Ca^{2+} can be released in an acidic environment, and more ROS can be produced in the combination of calcium overload and CDT/PTT/SDT for tumor therapy.

Detection of Intracellular Mitochondrial Membrane Potential

To verify the damage of Ca^{2+} and the synergistic treatment of Ca^{2+} and ROS on MMP, the decrease of MMP, a key index of mitochondrial damage, was detected by JC-10 staining.

As depicted in Figure 4B and C, the cells in the CTCH + Vc group exhibited subdued green fluorescence compared to the control group, indicating that Ca^{2+} may inhibit mitochondrial activity. In comparison to the CTCH + Vc group, the green fluorescence intensity of the CTCH group was heightened, suggesting that CTCH exerts a CDT effect and induces ROS-mediated mitochondrial apoptosis. Furthermore, when compared to the CTCH group, the green fluorescence intensity of the

CTCH + L group increased while the red fluorescence weakened, signifying that photothermal treatment with CTCH could enhance ROS production and consequently induce mitochondrial apoptosis. Similarly, an increase in green fluorescence intensity was observed in the CTCH + US group along with a decrease in red fluorescence, revealing that CTCH possesses SDT properties and can generate ROS to promote mitochondrial apoptosis. Notably, enhanced green fluorescence was evident in the CTCH + L + US group, indicating that calcium overload combined with CDT/PTT/SDT synergistic treatment could lead to substantial ROS generation and induction of mitochondrial apoptosis. HeLa cells treated with CTCH + L + US (pH = 6.5) displayed maximal green fluorescence intensity, denoting a significant reduction in MMP and severe mitochondrial damage. These findings suggest that elevated intracellular Ca^{2+} concentration induced by CTCH + L + US (pH = 6.5) can effectively cause mitochondrial dysfunction. Overall, the results indicate that under acidic conditions calcium overload combined with CDT/PTT/SDT synergistic effects could result in increased ROS production leading to reduced MMP and mitochondrial apoptosis, achieving effective tumor therapy.

Cytotoxicity Measurements of CTCH

HcerEpiC cells were used to evaluate the intracellular biosafety of CTCH. The survival rate of HcerEpiC cells after incubation with CuS, TAPP, or CTCH for 12 h was above 80% (Figure 4D). After treatment with ultrasound, laser irradiation, or both, there was almost no damage to HcerEpiC cells, suggesting that the material has biological safety demonstrating excellent biosafety of the material (Figure 4E).

The killing effect of CTCH on HeLa cells was further evaluated (Figure 4F). Vitamin C (Vc) was used to inhibit the CDT of CTCH for detecting the therapeutic effect of calcium overload, and the dark toxicity of CTCH was used to detect the killing effect of the synergistic effect of calcium overload and CDT. The cells were treated with ultrasound (CTCH+US group), 808 nm laser irradiation (CTCH+L group), or both (CTCH+US+L group) to evaluate the effects of SDT, PTT, and synergistic therapy. At a specific concentration of CTCH (50 μg/mL), the cellular viability under conditions of calcium overload was 63.93%, whereas the survival rate of the cells in the CTCH+US+L group was only 32.43%. Additionally, the survival rate of cells in the CTCH+US+L group was 20% under acidic conditions (pH = 6.5). These results indicate that CTCH released more Ca^{2+} in an acidic environment, which enhances the killing effect of CDT.

The killing effect of CTCH on HeLa cells was also evaluated visually by Calcein-AM/PI double staining (Figure 4G). The cells in the control group showed green fluorescence, indicating good cell viability. In the CTCH group, the green fluorescence decreased and the red fluorescence increased, which demonstrated partial cell death. This might be because CTCH had the synergistic therapeutic effect of calcium overload and CDT. Compared with the CTCH group, CTCH + L and CTCH + US groups showed weaker green fluorescence and greater red fluorescence, indicating that CTCH had good PTT and SDT effects. The cells in the CTCH + L + US group showed even stronger red fluorescence, suggesting that the synergistic therapy of calcium overload and CDT/PTT/SDT significantly enhanced the killing effect of the tumor. There was almost no green fluorescence in the CTCH + L + US group (pH = 6.5), indicating that calcium overload and CDT/PTT/SDT synergistic treatment exhibited the most obvious killing effect on tumor under acidic conditions. Figure 4H showed the corresponding quantization of the fluorescence intensity. The above results were consistent with the MTT results.

In vivo Combined Antitumor Efficacy Evaluation

Biochemical indexes, such as AST, ALT, Cr and BUN were selected to evaluate the liver and kidney function of the five groups. Liver and kidney function indexes did not show statistically significant differences among the five groups, suggesting that CTCH has a favorable biosafety (Figure S9). After the nude mice were euthanized, the hearts, livers, spleens, lungs, and kidneys of mice from each group were then collected for further analysis by pathological sections. No obvious abnormalities were found in all organs of the five groups, which further indicates that the physical stimulation and CTCH in the experiment will not cause tissue damage and CTCH has good biosecurity (Figure S10). Blood was collected from the eyeballs of nude mice during anesthesia, and the biocompatibility of CTCH was studied by using blood cells. Compared with the positive control group, as the concentration of CTCH increased, CTCH showed only weak hemolysis, indicating that CTCH exhibits good biocompatibility in the blood (Figure S11) and could be used as a tumor drug.

Infrared thermal imager was used to take thermal pictures at different times after caudal vein injection for the study of the tumor accumulation capability. With the extension of time (Figure 5A), the temperature gradually increased, reached the highest level (55°C) after 8 h of drug ingestion, and then gradually decreased, which may be due to drug metabolism.

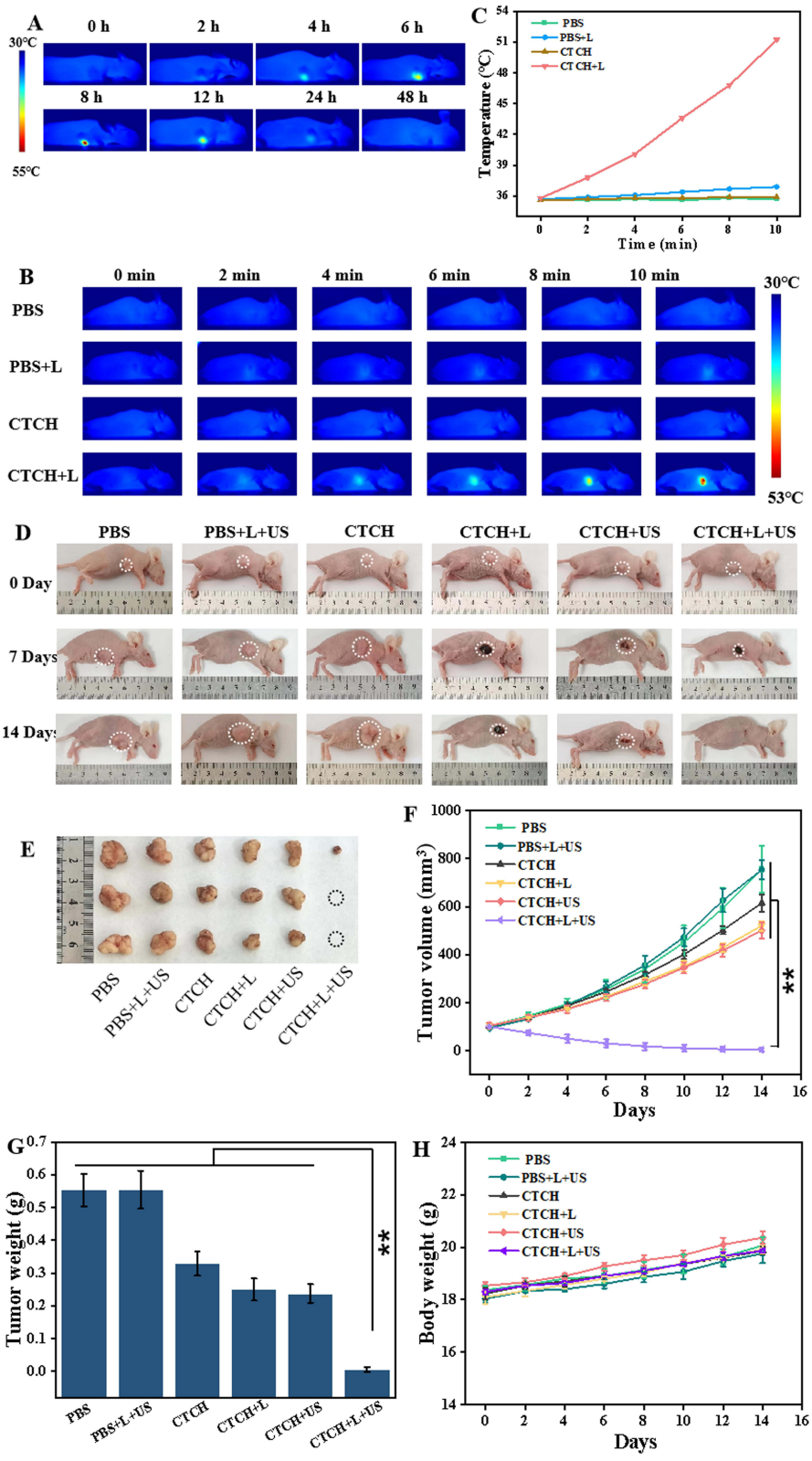

Figure 5 In vivo accumulation in tumor and photothermal capability of CTCH. (**A**) In vivo fluorescence images of tumor-bearing mice after intravenous injection with CTCH at different time points; (**B**) Photothermal imaging of CTCH in vivo; (**C**) Photothermal statistics in vivo; (**D**) Pictures of each group recorded at day 0, 7, and 14 during the treatment period; (**E**) Representative tumor images from each group after treatment; (**F**) Tumor volume changes of each group during treatment (**$P < 0.01$); (**G**) The tumor weight in each group after treatment (**$P < 0.01$); (**H**) The body-weight change of nude mice during treatment.

In vitro experiments showed good PTT properties of CTCH. In order to further study, the photothermal effect of CTCH in vivo, CTCH was injected through the caudal vein for 8 h and then irradiated with an 808 nm laser (1.5 W/cm^2) for 10 min (Figure 5B). No significant temperature change was found in the PBS, PBS + L, and CTCH group, while the temperature of the tumor site in the experimental group increased to 52°C. The corresponding temperature curve indicates that CTCH possessed great photothermal imaging ability (Figure 5C).

When the tumor volume of the nude mice reached about 100 mm^3, they were randomly divided into six groups composed of PBS, PBS + L + US, CTCH, CTCH + L, CTCH + US, and CTCH + L + US. After intravenous injection of CTCH, the CTCH + L, the CTCH + US, and CTCH + L + US groups were irradiated with 808 nm laser (1.5 W/cm^2) for 10 min, treated with ultrasound (0.8 W/cm^2) for 5 min and both laser and ultrasound, respectively. Figures 5D–F showed that the tumor volume in the PBS group and the PBS + L + US group increased to 755 mm^3 during the 14-day treatment period.

In the CTCH group, the tumor volume increased to 610 mm^3 induced by CDT treatment. Additionally, the tumor volume in CTCH + L and CTCH + US groups decreased significantly and reached 500 mm^3 originating from the effect of the PTT or SDT. Compared with the control group, the tumor weight in the CTCH + L + US group was close to zero, indicating that the tumor was almost eliminated in the CTCH + L + US group (Figure 5G). The changes in both tumor volume and tumor weight demonstrate excellent antitumor effects of CTCH. More importantly, the body weight of nude mice in the six groups increased slightly during treatment and no death occurred (Figure 5H), indicating that CTCH has good biocompatibility.

Conclusion

In this study, pH-responsive nanomaterial CTCH was designed and synthesized to enable collaborative, targeted and biosafe cancer therapy. Under acidic environment and excessive H_2O_2, CTCH can produce ·OH, and CTCH also has the properties of PTT and SDT. Cell experiments have shown that CTCH can effectively respond to TEM and release Ca^{2+} to further enhance the mitochondrial damage induced by calcium overload, thus having a more obvious killing ability on cancer cells. In vivo experiments in mice have proved that CTCH has good anti-tumor effect, and there is no obvious pathological damage in the tissue sections, and CTCH has good biocompatibility. The construction of CTCH nanomedical drugs provides a new therapeutic strategy for the treatment of tumor in response to the acidic environment of tumor, which is of great significance.

Acknowledgments

This study was financially supported by the Ministry of Science and Technology of China (973 Project No. 2021YFA1200600), the National Natural Science Foundation of China (Nos. 52231007, 51725101, 11727807, 82071969), Science Foundation of Shanxi Province (No. 202203021211236, 20210302123294, 202203021212375), Shanxi Province Doctoral Start-up Fund (No. SD2240), Science Research Start-up Fund for Doctor of Shanxi Medical University (XD2213), and Shanxi Province Higher Education Innovation Project (No. 2022L117).

Disclosure

The authors declare no competing interest in this work.

References

1. Burmeister CA, Khan SF, Schäfer G, et al. Cervical cancer therapies: current challenges and future perspectives. *Tumour Virus Res*. 2022;13:200238. doi:10.1016/j.tvr.2022.200238
2. Perkins RB, Wentzensen N, Guido RS, Schiffman M. Cervical cancer screening: a review. *JAMA*. 2023;330(6):547–558. doi:10.1001/jama.2023.13174
3. Matsuo K, Nusbaum DJ, Matsuzaki S, et al. Utilization and outcomes of adjuvant systemic chemotherapy alone in high risk, early stage cervical cancer in the United States. *Int J Gynecol Cancer*. 2021;31(7):991–1000. doi:10.1136/ijgc-2021-002655
4. Turinetto M, Valsecchi AA, Tuninetti V, Scotto G, Borella F, Valabrega G. Immunotherapy for cervical cancer: are we ready for prime time? *Int J Mol Sci*. 2022;23(7):3559. doi:10.3390/ijms23073559
5. De Las Rivas J, Brozovic A, Izraely S, Casas-Pais A, Witz IP, Figueroa A. Cancer drug resistance induced by EMT: novel therapeutic strategies. *Arch Toxicol*. 2021;95(7):2279–2297. doi:10.1007/s00204-021-03063-7
6. Zhang T, Lin R, Wu H, Jiang X, Gao J. Mesenchymal stem cells: a living carrier for active tumor-targeted delivery. *Adv Drug Deliv Rev*. 2022;185:114300. doi:10.1016/j.addr.2022.114300
7. Pouliquen DL, Malloci M, Boissard A, Henry C, Guette C. Proteomes of residual tumors in curcumin-treated rats reveal changes in microenvironment/malignant cell crosstalk in a highly invasive model of mesothelioma. *Int J Mol Sci*. 2022;23(22):13732. doi:10.3390/ijms232213732

8. Chen Q, Ma Y, Bai P, et al. Tumor microenvironment-responsive nanococktails for synergistic enhancement of cancer treatment via cascade reactions. *ACS Appl Mater Interfaces*. 2021;13(4):4861–4873. doi:10.1021/acsami.0c20268
9. Gao Y, Zhou H, Liu G, Wu J, Yuan Y, Shang A. Tumor microenvironment: lactic acid promotes tumor development. *J Immunol Res*. 2022;2022:3119375. doi:10.1155/2022/3119375
10. Chen D, Liu X, Lu X, Tian J. Nanoparticle drug delivery systems for synergistic delivery of tumor therapy. *Front Pharmacol*. 2023;14:1111991. doi:10.3389/fphar.2023.1111991
11. Gao Y, Wang K, Zhang J, Duan X, Sun Q, Men K. Multifunctional nanoparticle for cancer therapy. *MedComm*. 2023;4(1):e187. doi:10.1002/mco2.187
12. Niedźwiedzka-Rystwej P, Bębnowska D, Kołacz R, Deptuła W. Mitochondria, pattern recognition receptors and autophagy under physiological and pathological conditions, including viral infections. *Acta Biochim Pol*. 2021;69(1):1–10. doi:10.18388/abp.2020_5807
13. Zhang S, Zheng H, Yang L, Li Z, Yu M. NIR mitochondrial fluorescent probe for visualizing SO_2/polarity in drug induced inflammatory mice. *Anal Chem*. 2023;95(12):5377–5383. doi:10.1021/acs.analchem.2c05737
14. Wang C, Li T, Wang Z, et al. Nano-modulators with the function of disrupting mitochondrial Ca^{2+} homeostasis and photothermal conversion for synergistic breast cancer therapy. *J Nanobiotechnology*. 2023;21(1):465. doi:10.1186/s12951-023-02220-7
15. Wang W, Zhang Y, Wang Z, Liu X, Lu S, Hu X. A native drug-free macromolecular therapeutic to trigger mutual reinforcing of endoplasmic reticulum stress and mitochondrial dysfunction for cancer treatment. *ACS Nano*. 2023;17(11):11023–11038. doi:10.1021/acsnano.3c03450
16. Nguyen Cao TG, Truong Hoang Q, Hong EJ, et al. Mitochondria-targeting sonosensitizer-loaded extracellular vesicles for chemo-sonodynamic therapy. *J Control Release*. 2023;354:651–663. doi:10.1016/j.jconrel.2023.01.044
17. Khan MW, Zou C, Hassan S, et al. Cisplatin and oleanolic acid co-loaded pH-sensitive $CaCO_3$ nanoparticles for synergistic chemotherapy. *RSC Adv*. 2022;12(23):14808–14818. doi:10.1039/d2ra00742h
18. Dong Z, Feng L, Hao Y, et al. Synthesis of hollow biomineralized $CaCO_3$-polydopamine nanoparticles for multimodal imaging-guided cancer photodynamic therapy with reduced skin photosensitivity. *J Am Chem Soc*. 2018;140(6):2165–2178. doi:10.1021/jacs.7b11036
19. Zhang A, Xiao Z, Liu Q, et al. $CaCO_3$-encapuslated microspheres for enhanced transhepatic arterial embolization treatment of hepatocellular carcinoma. *Adv Healthc Mater*. 2021;10(19):e2100748. doi:10.1002/adhm.202100748
20. Zhao LP, Zheng RR, Chen HQ, et al. Self-delivery nanomedicine for O_2-economized photodynamic tumor therapy. *Nano Lett*. 2020;20(3):2062–2071. doi:10.1021/acs.nanolett.0c00047
21. Wang J, Kong W, Jin H, et al. Tumor microenvironment responsive theranostic agent for enhanced chemo/chemodynamic/photothermal therapy. *Colloids Surf B*. 2022;218:112750. doi:10.1016/j.colsurfb.2022.112750
22. Hwang E, Jung HS. Metal-organic complex-based chemodynamic therapy agents for cancer therapy. *Chem Commun*. 2020;56(60):8332–8341. doi:10.1039/d0cc03012k
23. Zhou L, Chen J, Sun Y, et al. A self-amplified nanocatalytic system for achieving "1 + 1 + 1 > 3" chemodynamic therapy on triple negative breast cancer. *J Nanobiotechnology*. 2021;19(1):261. doi:10.1186/s12951-021-00998-y
24. Wang Y, Zhang S, Wang J, et al. Ferrocene-containing polymersome nanoreactors for synergistically amplified tumor-specific chemodynamic therapy. *J Control Release*. 2021;333:500–510. doi:10.1016/j.jconrel.2021.04.007
25. Wang P, Liang C, Zhu J, et al. Manganese-based nanoplatform as metal ion-enhanced ROS generator for combined chemodynamic/photodynamic therapy. *ACS Appl Mater Interfaces*. 2019;11(44):41140–41147. doi:10.1021/acsami.9b16617
26. Ming L, Song L, Xu J, et al. Smart manganese dioxide-based lanthanide nanoprobes for triple-negative breast cancer precise gene synergistic chemodynamic therapy. *ACS Appl Mater Interfaces*. 2021;13(30):35444–35455. doi:10.1021/acsami.1c08927
27. Wibrianto A, Getachew G, Direrssa WB, et al. A multifunctional nanocatalyst based on ultra-fluorescent carbon quantum dots for cascade enzymatic activity and stimuli-responsive chemotherapy of cancer. *Carbon*. 2023;208:191–207. doi:10.1016/j.carbon.2023.03.052
28. Hu C, Hou B, Xie S. Application of nanosonosensitizer materials in cancer sono-dynamic therapy. *RSC Adv*. 2022;12(35):22722–22747. doi:10.1039/d2ra03786f
29. Kumar Yadav A, Kumar N, Talim Khan A, Kushwaha R, Banerjee S. Sonodynamic therapy with metal complexes: a new promise in cancer therapy. *ChemMedChem*. 2022;17(2):e202100615. doi:10.1002/cmdc.202100615
30. Liang S, Yao J, Liu D, Rao L, Chen X, Wang Z. Harnessing nanomaterials for cancer sonodynamic immunotherapy. *Adv Mater*. 2023;35(33):e2211130. doi:10.1002/adma.202211130
31. Zhao C, Pang X, Yang Z, Wang S, Deng H, Chen X. Nanomaterials targeting tumor associated macrophages for cancer immunotherapy. *J Control Release*. 2022;341:272–284. doi:10.1016/j.jconrel.2021.11.028
32. Jiang J, Huang Y, Zeng Z, Zhao C. Harnessing engineered immune cells and bacteria as drug carriers for cancer immunotherapy. *ACS Nano*. 2023;17(2):843–884. doi:10.1021/acsnano.2c07607
33. Liu S, Pan X, Liu H. Two-dimensional nanomaterials for photothermal therapy. *Angew Chem Int Ed Engl*. 2020;59(15):5890–5900. doi:10.1002/anie.201911477
34. Kizhepat S, Rasal AS, Chang JY, Wu HF. Development of two-dimensional functional nanomaterials for biosensor applications: opportunities, challenges, and future prospects. *Nanomaterials*. 2023;13(9):1520. doi:10.3390/nano13091520
35. Getachew G, Wibrianto A, Rasal AS, et al. Metal halide perovskite nanocrystals for biomedical engineering: recent advances, challenges, and future perspectives. *Coordin Chem Rev*. 2023;482:215073. doi:10.1016/j.ccr.2023.215073
36. Getachew G, Huang WW, Chou TH, Rasal AS, Chang JY. Brightly luminescent (NH4)xCs1-xPbBr3 quantum dots for in vitro imaging and efficient photothermal ablation therapy. *J Colloid Interface Sci*. 2022;605:500–512. doi:10.1016/j.jcis.2021.07.116
37. Getachew G, Hsiao CH, Wibrianto A, et al. High performance carbon dots based prodrug Platform: image-Guided photodynamic and chemotherapy with on-demand drug release upon laser irradiation. *J Colloid Interface Sci*. 2023;633:396–410. doi:10.1016/j.jcis.2022.11.112
38. Getachew G, Tien YC, Kan TC, et al. Defect-passivated metal halide perovskite quantum dots stabilized into biodegradable porous polydopamine nanoparticles for photothermal/chemodynamic/gas therapy of cancer. *Chem Eng J*. 2023;467:143560. doi:10.1016/j.cej.2023.143560
39. Shendage SS, Ingole VH, Rasal A, et al. Sustainable development of a bioactive material from recycled rice husk and eggshell for bone regeneration application. *ACS Sustain Chem Eng*. 2024;12(7):2598–2610. doi:10.1021/acssuschemeng.3c06290
40. Korupalli C, Kuo CC, Getachew G, et al. Multifunctional manganese oxide-based nanocomposite theranostic agent with glucose/light-responsive singlet oxygen generation and dual-modal imaging for cancer treatment. *J Colloid Interface Sci*. 2023;643:373–384. doi:10.1016/j.jcis.2023.04.049

41. Li B, Yuan F, He G, et al. Ultrasmall $CuCo_2S_4$ nanocrystals: all-in-one theragnosis nanoplatform with magnetic resonance/near-infrared imaging for efficiently photothermal therapy of tumors. *Adv Funct Mater*. 2017;27(10):1606218. doi:10.1002/adfm.201606218
42. Xu L, Tong G, Song Q, et al. Enhanced intracellular Ca^{2+} nanogenerator for tumor-specific synergistic therapy via disruption of mitochondrial Ca^{2+} homeostasis and photothermal therapy. *ACS Nano*. 2023;17(22):23220. doi:10.1021/acsnano.3c10523
43. Min H, Qi Y, Zhang Y, et al. A graphdiyne oxide-based iron sponge with photothermally enhanced tumor-specific Fenton chemistry. *Adv Mater*. 2020;32(31):e2000038. doi:10.1002/adma.202000038